

**ThesisTitle**

by

**Daniel C. Cole**

Other Degrees

A thesis submitted to the  
Faculty of the Graduate School of the  
University of Colorado in partial fulfillment  
of the requirements for the degree of  
Doctor of Philosophy  
Physics Physics  
2018

This thesis entitled:  
ThesisTitle  
written by Daniel C. Cole  
has been approved for the Physics Physics

---

Reader1

---

Reader2

Date \_\_\_\_\_

The final copy of this thesis has been examined by the signatories, and we find that both the content and the form meet acceptable presentation standards of scholarly work in the above mentioned discipline.

Cole, Daniel C. (Ph.D., Physics)

ThesisTitle

Thesis directed by Dr. Scott A. Diddams

Optical frequency combs have revolutionized precision metrology by enabling measurements of optical frequencies, with implications both for fundamental scientific questions and for applications such as fast, broadband spectroscopy. In this thesis, I describe the development of comb generation platforms with smaller footprints and higher repetition rates, with the ultimate goal of bringing frequency combs to new applications in a chip-integrated package. I present two new types of frequency combs: electro-optic modulation (EOM) combs and Kerr-microresonator-based frequency combs (microcombs). First I describe the EOM comb scheme and, in particular, techniques for mitigating noise in the comb generation process, and I present the results of a proof-of-principle metrology experiment and some possible applications. Then I discuss developments in microcomb technology. I present novel soliton crystal states, which have highly structured fingerprint optical spectra that correspond to ordered pulse trains exhibiting crystallographic defects. These pulse trains arise through interaction of the solitons with avoided mode-crossings in the resonator spectrum. Next, I describe the direct and deterministic generation of single microresonator solitons using a phase-modulated pump laser. This technique removes the dependence on initial conditions that was formerly a universal feature of these experiments, presenting a solution to a significant technical barrier to the practical application of microcombs. I also discuss generation of Kerr combs in the Fabry-Perot (FP) geometry. I introduce a nonlinear partial differential equation describing dynamics in an FP cavity and discuss the differences between the FP geometry and the ring cavity, which is the geometry used in previous Kerr-comb experiments. Finally, I discuss a technique for reducing the repetition rate of a high-repetition-rate frequency comb, which will be a necessary post-processing step for some applications. I conclude with a discussion of avenues for future research, including the chip-integration of Fabry-Perot Kerr resonators and the use of band-engineered photonic crystal cavities to further simplify soliton generation.

## Acknowledgements

The work in this thesis would not have been possible...

- Acknowledgement line 1
- Acknowledgement line 2

## Contents

<b>1</b>	<b>PM Pumping</b>	<b>1</b>
1.1	Theoretical investigation of soliton generation with a phase-modulated pump laser . . . . .	1
1.2	Spontaneous generation of single solitons using a phase-modulated pump laser . . . . .	4
1.3	Soliton control using a phase-modulated pump laser . . . . .	6
1.4	Subharmonic phase modulation for high repetition-rate systems . . . . .	9
<b>2</b>	<b>Soliton Crystals</b>	<b>11</b>
2.1	Mechanism of soliton crystallization . . . . .	12
2.1.1	Simulation of soliton crystals . . . . .	16
2.2	Case study: pair distribution function for a superstructured crystal . . . . .	17
2.3	Soliton crystal configuration space . . . . .	20
<b>References</b>		<b>23</b>

## Figures

1.1	Figure Title . . . . .	2
1.2	Figure Title . . . . .	3
1.3	Figure Title . . . . .	5
1.4	Figure Title . . . . .	6
1.5	Figure Title . . . . .	7
1.6	Figure Title . . . . .	8
1.7	Figure Title . . . . .	10
2.1	Generation and characterization of a soliton crystal . . . . .	13
2.2	Stabilization and collapse of a soliton crystal . . . . .	17
2.3	Spectrum and waveform of a superstructured soliton crystal . . . . .	18
2.4	Simulated generation of a superstructured soliton crystal . . . . .	19
2.5	Pair distribution function for soliton crystal generation . . . . .	20
2.6	Taxonomy of soliton crystals . . . . .	22

# Chapter 1

## PM Pumping

This chapter discusses the direct generation and control of single solitons in optical microring resonators using a pump-laser phase modulated at a frequency near the resonator's free spectral range. Based on a proposal by Taheri, Eftekhar, and Adibi in 2015 [1], these experimental results represent a promising new method for simple and deterministic generation of single solitons.

To illustrate the utility of using a phase-modulated pump laser, we first present theoretical investigations into the effect of this phase modulation (PM), and then we present experimental results on the generation and control of single solitons.

### 1.1 Theoretical investigation of soliton generation with a phase-modulated pump laser

To theoretically explore the physics of soliton generation with PM pumping, we use the LLE with a modified driving term that incorporates the effect of phase modulation [1]:

$$\frac{\partial \psi}{\partial \tau} = -(1 + i\alpha)\psi + i|\psi|^2\psi - i\frac{\beta}{2}\frac{\partial^2 \psi}{\partial \theta^2} + Fe^{i\delta_{PM} \cos \theta}. \quad (1.1)$$

Here  $\delta_{PM}$  represents the phase-modulation index, where the resonator is driven by a field  $E_{PM} = E_0 e^{i\delta_{PM} \cos(2\pi f_{PM} t)}$ ;  $f_{PM} \sim f_{FSR}$  is the frequency of the applied phase modulation.

Simulations of Eq.1.1 reveal that PM transforms the resonator excitation spectrum from a series of  $N = 0, 1, 2, \dots$  up to  $N_{max}$  solitons to a single level  $N = 1$  near threshold, eliminating degeneracy between these states as shown in Fig. 1.1. This occurs due to amplitude variations resulting from

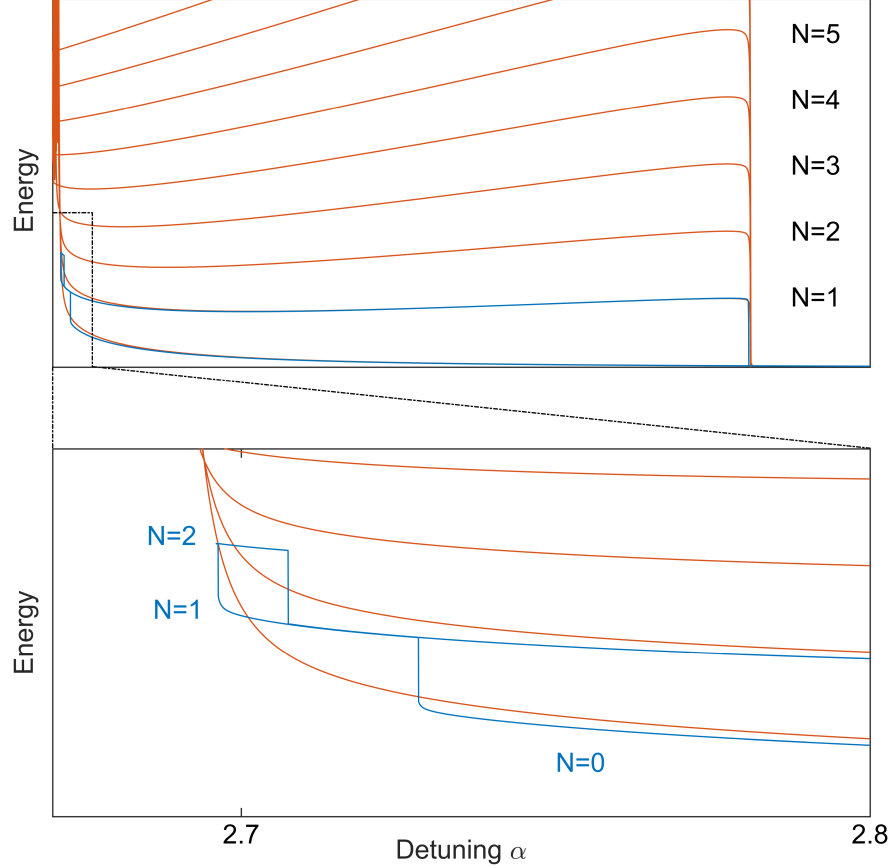


Figure 1.1: titletext

the phase modulation, with dispersion and nonlinearity providing PM-to-AM conversion. We can gain some insight into the origin of this effect by inserting the ansatz  $\psi(\theta, \tau) = \phi(\theta, \tau)e^{i\delta_{PM} \cos(\theta)}$  into Eq. 1.1 [2]. By expanding the second-derivative term and setting derivatives of  $\phi$  to zero<sup>1</sup> we arrive at an equation for the quasi-CW background in the PM-pumped resonator:

$$F = (\gamma(\theta) + i\eta(\theta)) \phi + i|\phi|^2 \phi, \quad (1.2)$$

where effective local loss and detuning terms have been defined as:

$$\gamma(\theta) = 1 + \frac{\beta_2}{2} \delta_{PM} \cos \theta, \quad (1.3)$$

$$\eta(\theta) = \alpha - \frac{\beta_2}{2} \delta_{PM}^2 \sin^2 \theta. \quad (1.4)$$

---

<sup>1</sup> We note the contribution of Miro Erkintalo in suggesting this approximation.

This equation immediately yields an approximation for the stationary solution  $\psi_s$ :

$$\psi_s = \frac{F e^{i\delta_{PM} \cos \theta}}{\gamma(\theta) + i(\eta(\theta) - \rho(\theta))}, \quad (1.5)$$

where  $\rho(\theta) = |\phi(\theta)|^2$  is the (smallest real) solution to the cubic polynomial that results from taking the modulus-square of Eq. 1.2:

$$F^2 = [\gamma(\theta)^2 + (\eta(\theta) - \rho(\theta))^2] \rho(\theta). \quad (1.6)$$

In neglecting spatial derivatives of  $\phi$  but retaining the derivatives of the phase term  $e^{i\delta_{PM} \cos \theta}$  we have made the approximation that the dominant effect of dispersion comes from its action on the existing broadband phase-modulation spectrum. This model reveals that amplitude variations in the quasi-CW background can be expected as a result of the spatially-varying effective loss and detuning terms that arise from the periodically-chirped pump laser.

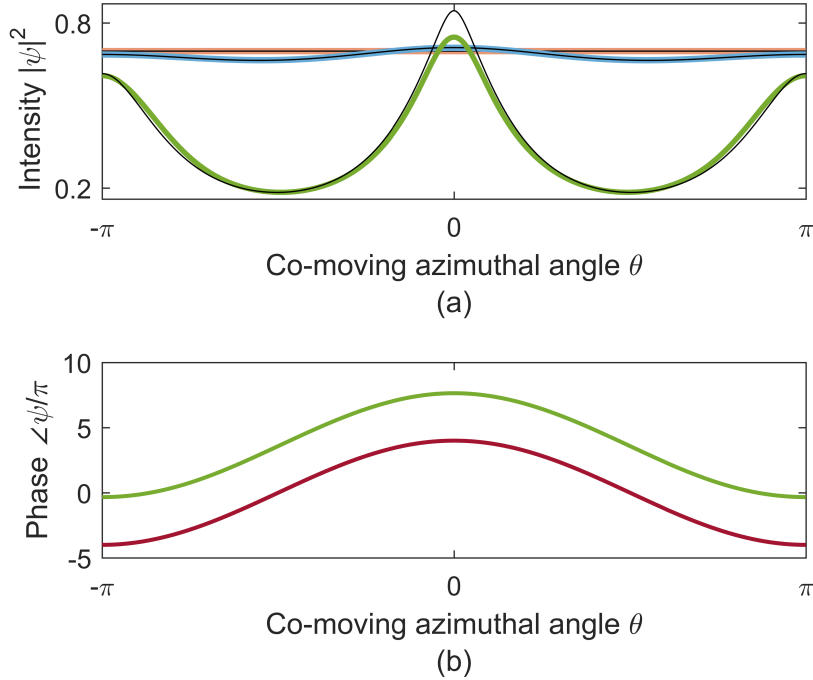


Figure 1.2: titletext

Fig. 1.2 compares the predictions of numerical LLE simulations (color) with the analytical model (black). The two agree quantitatively at small modulation depth ( $\delta_{PM} = \pi/2$ , blue) and

qualitatively at larger depth ( $\delta_{PM} = 4\pi$ , green). Both the simulations and the approximate analytic solution indicate that the background has two peaks per round trip in the presence of phase modulation, which suggests a mechanism for spontaneous single-soliton generation: At threshold the larger peak becomes locally unstable, and a soliton is formed by local modulation instability [3, 4]. Moreover, it is known that if solitons exist elsewhere they are pushed to the larger peak by the backgrounds modulated phase [2]. This makes superpositions of  $N > 1$  solitons unstable and practically forbidden. Generation of single solitons then simply requires tuning the pump power and frequency to appropriate values, regardless of initial conditions.

The detuning for soliton generation can be estimated using Eq. 1.2 by calculating the value of  $\alpha$  where  $\rho(\theta = 0) = 1$ . This comes with a further approximation, as simulations reveal that the critical detuning for soliton formation is near but not necessarily at  $\rho = 1$  because the spatial interval over which threshold is exceeded must have some minimum width. However, this approach quantitatively captures the behavior shown in Fig. 1.1, predicting soliton generation at  $\alpha = 2.737$ .

## 1.2 Spontaneous generation of single solitons using a phase-modulated pump laser

We demonstrate deterministic generation of single solitons without condensation from an extended pattern in a 22-GHz FSR silica ring resonator with  $\Delta\nu \sim 1.5$  MHz linewidth [5]. We generate a frequency-agile laser for pumping the resonator by passing a CW laser through a single-sideband modulator that is driven by a voltage-controlled oscillator [6]; the seed laser is extinguished in the modulator and the resulting sideband can be swept by . The pump laser is phase-modulated with index  $\delta_{PM} \sim \pi$  and amplified to normalized power  $F^2$  between 2 and 6. We are able to measure and control the pump-laser detuning in real time using an AOM-shifted probe beam as shown in Fig. ??, which allows thermal instabilities associated with the red detuning that is required for soliton generation to be overcome. The experimental setup and a frequency domain depiction of our locking scheme are shown in Fig. ??.

To generate single solitons, we begin with large red detuning  $\nu_0 - \nu_{pump} = 40$  MHz and decrease

rate and de-  
scription  
here

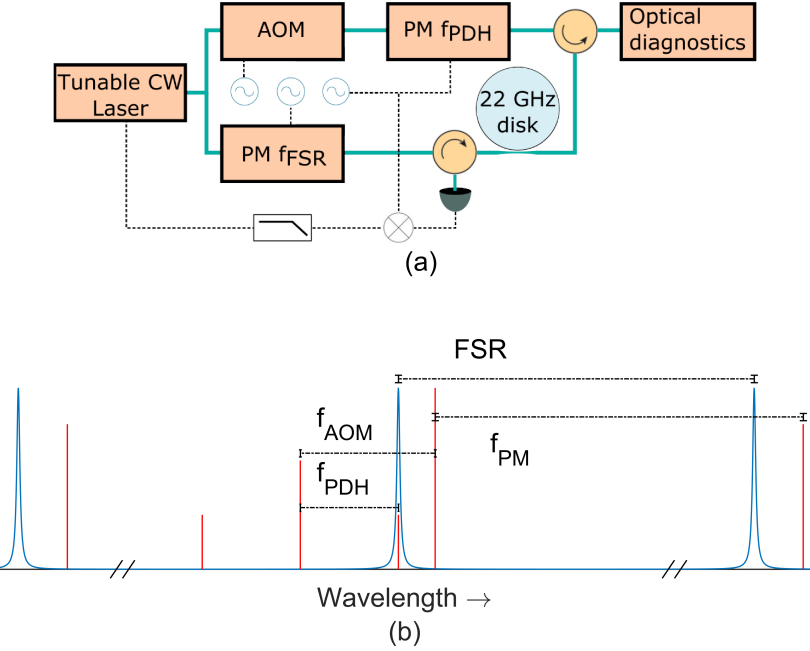


Figure 1.3: title text

the detuning until a soliton is generated near  $\nu_0 - \nu_{pump} \sim 5$  MHz detuning, where this value depends on the pump power and coupling condition. We measure the power converted by the Kerr nonlinearity to new frequencies by passing a portion of the resonator's output through an optical band-reject filter; this 'comb power' measurement reveals a step upon soliton formation, as shown in Fig. ???. After soliton generation, we observe that the soliton can be preserved while the detuning is increased again up to a maximum value near , consistent with Fig. ???. Additionally, we observe that it is possible to turn off the phase modulation without loss of the soliton, in agreement with the simulations presented in Ref. [1].

get from  
Jordan

Automating soliton generation by repeatedly scanning the laser into resonance ( $\nu_0 - \nu_{pump} \sim 5$  MHz) and back out again ( $\nu_0 - \nu_{pump} \sim 20$  MHz, far enough that the soliton is lost) has enabled reversible generation of 1000 solitons in 1000 trials over 100 seconds, with a measured 100 % success rate. Our probe beam allows measurement of the detuning at which soliton generation occurs, which changes little from run to run. We present a histogram of detuning measurements for the generation

of 160 solitons in Fig. ??.

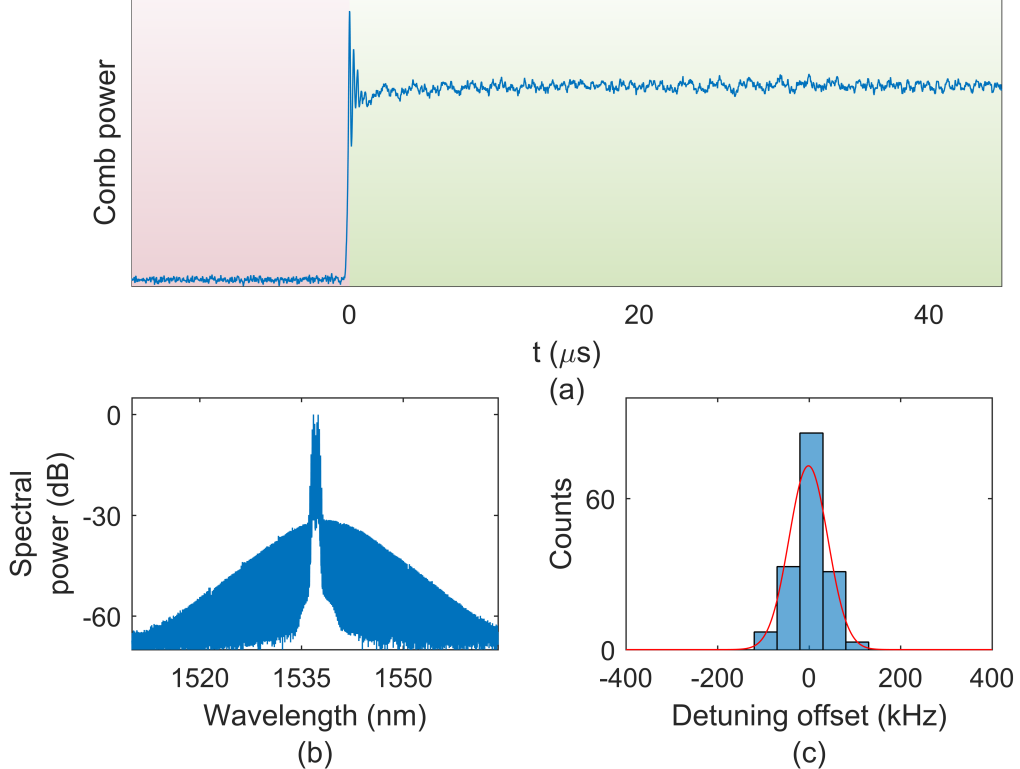


Figure 1.4: titletext

### 1.3 Soliton control using a phase-modulated pump laser

In addition to enabling deterministic generation of single solitons, phase modulation of the pump laser also facilitates timing and repetition-rate control of the resulting pulse train. In our experiments, the repetition rate of the out-coupled pulse train ( $f_{rep}$ ) remains locked to  $f_{PM}$  over a bandwidth of  $\pm 40$  kHz. This observation is consistent with an estimate of the locking range  $\delta_{PM} \times D_2/2\pi \sim 44$  kHz that is presented in Ref. [2], where we have used the approximate value  $D_2 = 14$  kHz/mode. Fig. ?? shows the measured repetition rate as  $f_{PM}$  is swept sinusoidally through a range of  $\pm 50$  kHz around the soliton's natural repetition rate; the repetition rate follows the PM except for glitches near the peaks of the sweep. In the inset of Fig. ?? we overlay the results of

LLE simulations that qualitatively match the observed behavior. These simulations are conducted by introducing the term  $+\beta_1 \frac{\partial\psi}{\partial\theta}$  to the right-hand side of Eq. 1.1, where  $\beta_1 = -2(f_{FSR} - f_{PM})/\Delta\nu$  incorporates a difference between the modulation frequency and the FSR of the resonator into the model;  $\beta_1$  may be varied in time to simulate the sweep of  $f_{PM}$ . These simulations indicate that the periodic nature of the glitches is due to the residual pulling of the phase modulation on the soliton when the latter periodically cycles through the pumps phase maximum.

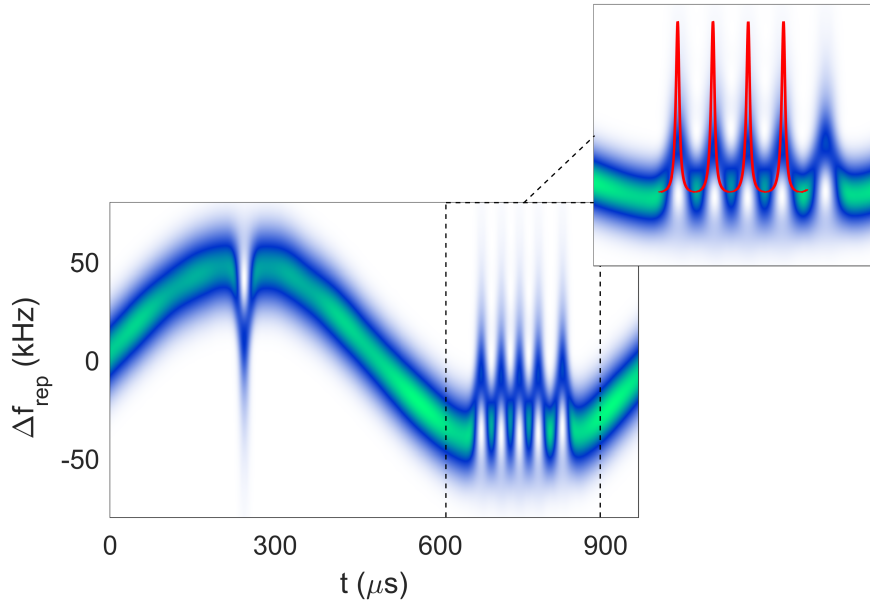


Figure 1.5: titletext

To evaluate the utility of phase modulation for fast control of the soliton's properties, we measure the repetition rate of the pulse train as  $f_{PM}$  is rapidly switched  $\pm 40$  kHz, within the soliton's locking range. This measurement is conducted by photodetecting the pulse train after removing the central spectral lines corresponding to the spectrum of the pump laser using an optical band-reject filter. In order to obtain a measurement trace of the repetition rate as a function of time, the photodetected signal is split and one path is sent through a reactive circuit element that induces a frequency-dependent phase shift. By comparing the phase between the two paths as a function of time, the time-dependent repetition rate can be determined.

We construct eye-diagrams out of the resulting data; these are shown in Fig. ???. In Fig. ??,m

$f_{PM}$  is switched with  $200 \mu\text{s}$  period and  $10 \mu\text{s}$  transition time; in Fig. ?? it is switched with  $100 \mu\text{s}$  period and  $60 \text{ ns}$  transition time. These eye diagrams show that the PM enables exquisite control of the soliton pulse train.

We overlay a simulated eye diagram on the data in Fig. ???. This simulation is conducted for parameters  $\Delta\nu = 1.5 \text{ MHz}$ ,  $\delta_{PM} = 0.9\pi$  that are near the experimental values, and the agreement between measurement and simulation indicates that the measurements are consistent with fundamental LLE dynamics. Fig. ?? presents the results of additional LLE simulations; the basic result is that the switching speed of  $f_{rep}$  is limited by the resonator linewidth, and can be only modestly improved by increasing  $\delta_{PM}$ .

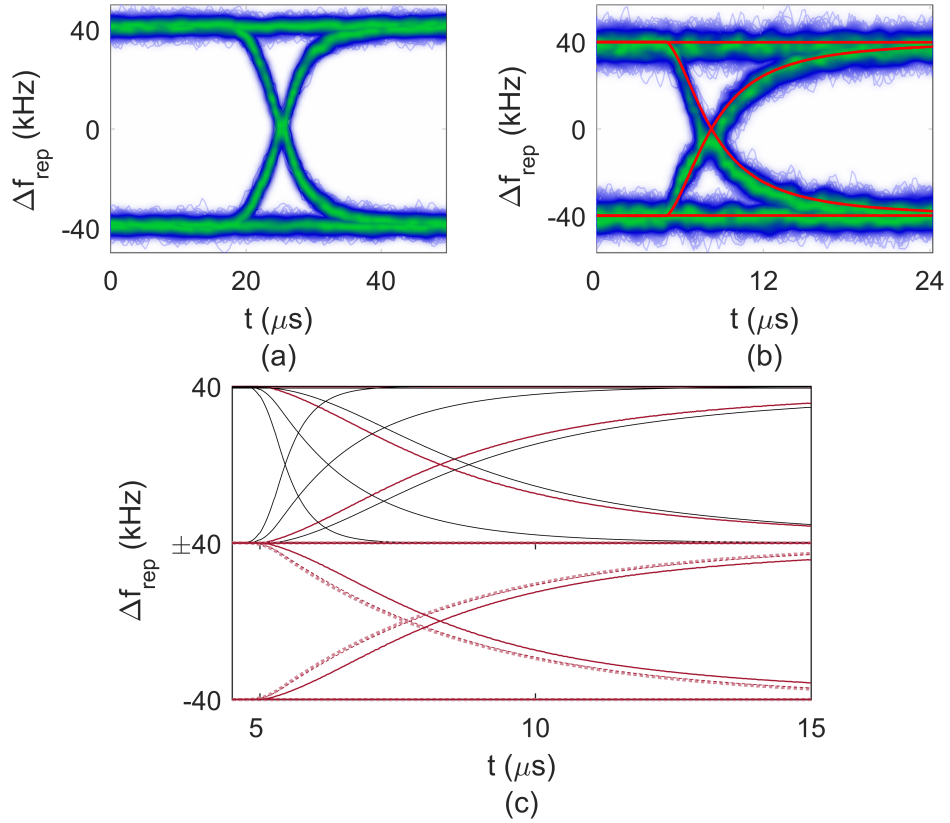


Figure 1.6: titletext

## 1.4 Subharmonic phase modulation for high repetition-rate systems

One apparent barrier to the use of a phase-modulated pump laser for protected single-soliton generation and manipulation is the electronically-inaccessible FSRs of some typical microcomb resonators. However, it is possible to overcome this challenge by phase modulating at a subharmonic of the FSR. Simulations indicate that PM can directly excite single solitons with small modulation depth, e.g.  $\delta_{PM} = 0.15\pi$ . In this limit, only the first-order PM sidebands are relevant, and their amplitude and phase relative to the carrier control the dynamics. For a small desired modulation depth defined by the relationship between the first-order sidebands and the carrier, it is possible to modulate at a frequency  $f_{mod} \sim f_{FSR}/N$  so that the  $N^{\text{th}}$ -order PM sidebands and the carrier address resonator modes with relative mode numbers -1, 0, and 1. The depth of modulation at the frequency  $f_{mod}$  can be chosen to fix the amplitudes of the  $N^{\text{th}}$ -order PM sidebands relative to the carrier and target a desired effective modulation depth. It is worth noting that when  $N$  is odd, phase modulation is recovered when the sidebands of order  $-N, 0$ , and  $N$  address resonator modes -1, 0, and 1. When  $N$  is even the result is pure amplitude modulation, such that the driving term takes the form  $F(1 + A \cos \theta)$ . Simulations indicate that this AM profile also enables spontaneous single-soliton generation under some circumstances, but we note that this modulation profile cannot be obtained from a standard Mach-Zehnder modulator, which provides a drive like  $F \cos(\eta + \delta \cos \theta)$ .

Fig. ?? presents an example of this technique. We simulate spontaneous soliton generation with PM at  $f_{mod} = f_{rep}/N = f_{rep}/21$ . The effective modulation depth is  $0.15\pi$ , which requires real modulation depth at the frequency  $f_{mod}$  with depth  $\delta_{PM} \sim 8.3\pi$ . Because the phase modulation spreads the optical power into the PM sidebands, use of this technique requires higher optical power for the same effective pumping strength; in this example the optical power must be increased by  $\sim 15.6$  dB. While the required modulation depth and pump power are higher with subharmonic phase modulation, neither is impractical. This technique could be used for spontaneous single-soliton generation in high-repetition rate systems; the example above indicates that it could be immediately applied in a 630 GHz-FSR resonator with 30 GHz phase modulation.

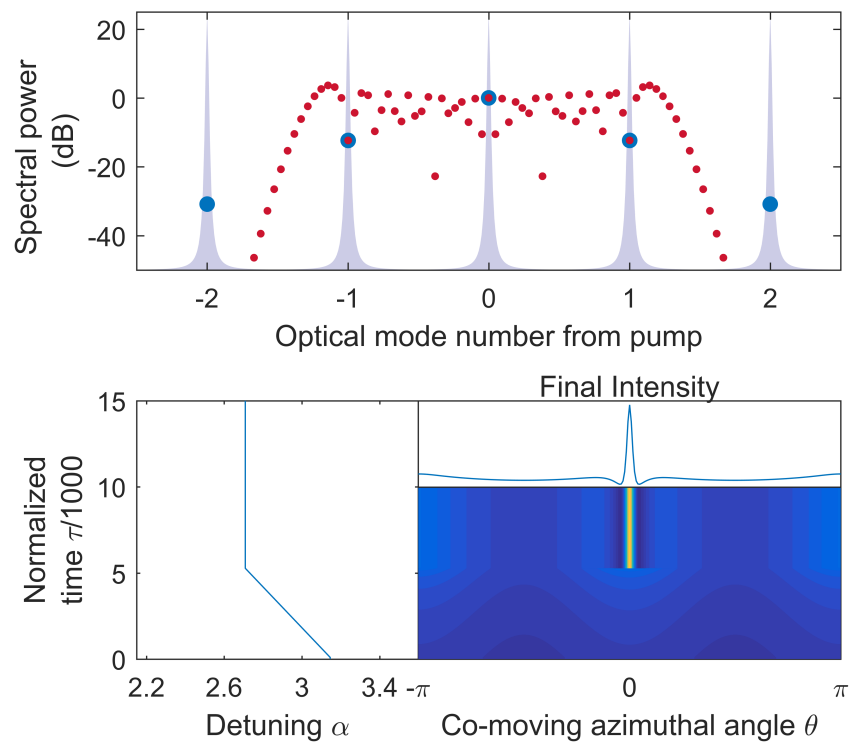


Figure 1.7: titletext

## Chapter 2

### Soliton Crystals

This chapter presents results on the self-organization of ensembles of solitons in optical microring resonators. The reported phenomenon explains physics that goes beyond the basic LLE model of Kerr-comb formation, as is described in Sec. ???. We refer to these self-organized ensembles as ‘soliton crystals,’ which extends an analogy to condensed-matter physics that has been made in other nonlinear-optical systems, including single-pass nonlinear fiber systems [7] and harmonically mode-locked fiber laser [8, 9], where a mechanism for soliton crystallization that is based on two distinct timescales of the laser medium [10] and is different from the one presented here was identified. Notably, the spatiotemporal chaos exhibited in the LLE was referred to as a ‘soliton gas’ in early studies of nonlinear dynamics in passive fiber-loop resonators [11–13].

Soliton crystals are soliton ensembles in which each soliton lies on a lattice site  $\theta_n = 2\pi n/N$  in the azimuthal co-moving frame, where  $N$  is a lattice parameter that arises from the fundamental physics of the system as described below and  $n$  indexes over the lattice sites. In a typical soliton crystal, there are many more available lattice sites than solitons, so that a fraction of the lattice sites are occupied. In the frequency domain, the temporal ordering of soliton crystals corresponds to highly modulated optical spectra that exhibit distinct features; we present an example spectrum in Fig. ??, where we demonstrate that the characteristic nature of the crystal spectrum is destroyed upon small random displacement of the solitons from their lattice sites. We have observed a wide variety of crystal configurations, and we present some of them in Sec. ??; to characterize this highly-degenerate configuration space we adopt terminology from condensed matter physics to describe

figure

soliton crystal structure and defects.

Soliton crystals are characterized by stable, dense occupation of the resonator by soliton pulses, and this dense occupation comes with high circulating power relative to single solitons or few-soliton ensembles. This important fact allows soliton crystals to be generated with decreasing pump-laser frequency scans across the resonance that are adiabatic—slow enough that both the resonator temperature and the state of the comb  $\psi$  are maintained at values<sup>1</sup> that correspond to the instantaneous  $\alpha$  and  $F^2$  parameters throughout the scan. We demonstrate generation of a soliton crystal in a slow scan in Fig. 2.1; it is useful to contrast this with the behavior exhibited in Fig. ??.

## 2.1 Mechanism of soliton crystallization

Fig. 2.1c presents the optical spectrum and corresponding time-domain simulation of a soliton crystal. This spectrum consists of widely-spaced primary-comb lines that are separated by many resonator FSR, superposed on top of an underlying  $\text{sech}^2$  spectrum of the kind that corresponds to a single soliton. In fact, this spectrum can be understood through the basic superposition principle of the electric field: The primary comb spectrum with spacing  $N \times f_{\text{FSR}}$  corresponds to a train of  $N$  uniformly spaced pulses in the resonator. The observed crystal spectrum corresponds to such a pulse train with a single vacancy, where a pulse is missing. The effect of this vacancy on the spectrum can be understood by considering the addition of an *out-of-phase* pulse  $S_-$  to a primary-comb pulse train that coincides in time with one of the existing pulses—in the time domain this corresponds to removal of one of the pulses, while in the spectral domain this corresponds to the addition (in the phase-sensitive field quantity) of the primary-comb spectrum and the single, out-of-phase soliton. The soliton crystal spectrum shown in Fig. ?? can also be understood this way: If a second soliton  $S_+$  is added to the initial primary-comb pulse train, this one *in phase* with the existing pulses and slightly temporally shifted from the vacancy, the result is a pulse train with one pulse displaced from its expected position based on uniform spacing. In the frequency domain, the positions of the pulses

---

<sup>1</sup> This terminology is a bit imprecise when applied to chaotic Kerr-combs that evolve with time; in this case the chaos exhibits the same behavior at each point in the scan that would be expected if  $\alpha$  and  $F^2$  were held fixed.

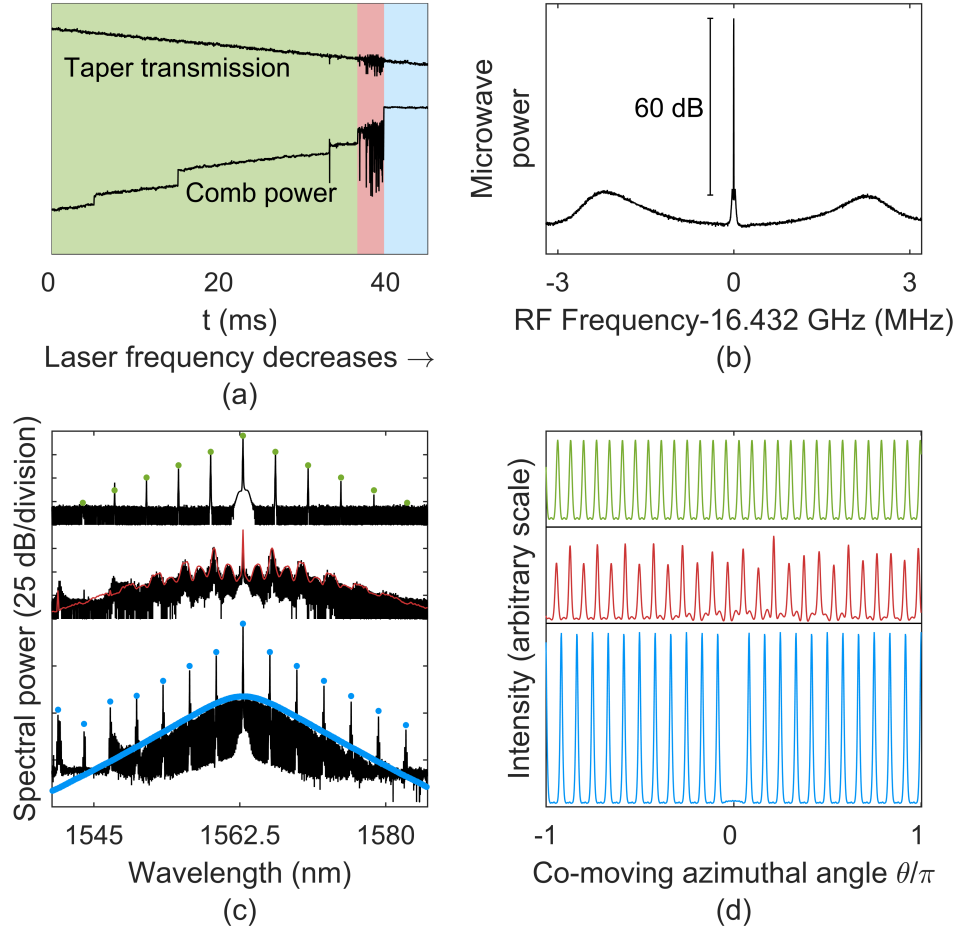


**Figure 2.1: Generation and characterization of a soliton crystal.** (a) Taper transmission and comb power during crystal generation with a scan that proceeds through primary-comb (green), chaotic (red), and soliton crystal (blue) regimes. The resonator's thermal response leads to the non-Lorentzian taper transmission profile, and the continuity of the taper transmission trace upon soliton crystal condensation indicates that the intracavity power of the soliton crystal is matched to the chaos that precedes it. (b) Narrow measured RF beat for the repetition rate of the soliton crystal is indicative of a coherent comb, in contrast with the chaotic state. (c) Progression of the optical spectrum through the scan, with experimental data (black) obtained by halting the scan at the appropriate point, and LLE simulations (with a perturbation as described in Sec. ??) in color. The simulated spectrum for the chaotic state shown in red is a time average. (d) Simulated time-domain traces corresponding to the simulated spectra in (c). This soliton crystal is a uniform pulse train with a single vacancy (see text).

$S_+$  and  $S_-$  correspond to a different linear spectral phase-shift on each of their individual spectra; when these spectra are added together (in the phase-sensitive field quantity) the result is spectral interference that is periodic in frequency. This gives rise to the lobes beneath the primary-comb lines; the period (in frequency) of the interference is inversely proportional to the separation between

the pulses  $S_+$  and  $S_-$  in time.

The simulated time-domain waveforms of the two crystals shown above are not stable in evolution under the LLE. For each, the observed width of the spectrum fixes the ratio between  $\alpha$  and  $\beta$ , as seen from Eq. ???. This ratio then fixes the temporal duration of the solitons, in turn determining the characteristic length of their interactions. When an attempt to simulate the crystal according to the LLE is made with parameters (e.g.  $F^2 = ??$ ,  $\alpha = ??$ , and  $\beta = ??$  for the crystal in Fig. 2.1) that give agreement with the measured width of the optical spectrum, it is found that pair-wise attractive interactions between solitons lead to collapse of the crystal.

A stabilization mechanism that goes beyond the physics of the LLE is responsible for the stability of this and other soliton crystals. The stabilization mechanism arises from avoided mode-crossings in the resonator spectrum. A ‘mode family’ corresponds to a set of circulating modes that have different azimuthal mode numbers but (approximately, neglecting wavelength-dependent effects) the same transverse spatial mode profile. As discussed in Sec. ???, some resonators support multiple mode families, each with its own free spectral range at a given wavelength. Although the modes in different families are in principle orthogonal, coupling between them can be provided by perturbations, for example by the coupling waveguide or tapered fiber used to drive the resonator. If a coupling exists between two modes that are sufficiently close in frequency, the frequencies of the modes become displaced from their frequencies in the absence of this coupling [Haus1991]. This affects Kerr-comb generation in the affected mode families, because the local detuning between the resonator modes and the Kerr-comb modes is changed as a result of the mode crossing. This comb-resonator detuning change may either enhance or inhibit nonlinear frequency conversion to the effected Kerr-comb modes, thereby changing the amplitude of these modes in the comb spectrum.

It has been reported that avoided mode crossings in the resonator spectrum can inhibit soliton generation in anomalous-dispersion resonators[4, 6], while they can facilitate the formation of Kerr-combs in normal-dispersion resonators[37] . Here we are interested specifically in the impact of the avoided mode crossing on the waveform of a soliton. For simplicity, we focus on the case where a single comb mode is affected by the mode crossing. When the change in the comb-resonator

other citations here

detuning increases the amplitude of that mode in the soliton's spectrum, the change to the time-domain waveform can be understood by considering this increase as the addition of extra CW light at the frequency of that mode. This extra CW light exists throughout the cavity, and it leads the introduction of periodic intensity oscillations in the background on which the soliton rides as the new CW light beats against the existing background at the pump frequency. This new background wave in the cavity has a period of  $2\pi/\mu_x$  in the angular coordinate  $\theta$ , where  $\mu_x$  is the pump-referenced mode number of the Kerr-comb mode affected by the mode crossing, for which the detuning has been shifted.

When several of these perturbed solitons co-propagate in a resonator, they interact through their extended waves and arrange themselves such that the waves constructively interfere. Each soliton then lies at the peak of a single extended background wave in the resonator, similar to predictions for bichromatically pumped Kerr combs[38]. Importantly, temporal separations between solitons are therefore required to be multiples of this wave's period, and the wave stabilizes the crystal against the attractive interactions discussed above. Furthermore, the wave's amplitude, and thus the strength of the crystal against perturbations, increases with the number of co-propagating perturbed solitons. Finally, we note that at least within the assumption of single-mode perturbation of the comb's spectrum, this interaction has infinite range.

We note that the mechanism observed here builds on previous reports of related phenomena. It has been shown that local interactions between cavity solitons can arise through decaying oscillatory tails [39], leading to the formation of small, locally ordered soliton molecules. Furthermore, it has been shown that the injection of an additional CW laser into a passive fiber-ring resonator can result in the generation of uniform distributions of solitons [40]. The mechanism we report here can be viewed as a variant of this CW-soliton interaction in which the ‘injected’ CW laser is provided by the affect of the mode crossing on the solitons' spectra.

We connect this discussion to the soliton-crystal spectrum presented in the bottom trace of Fig. 2.1c—this spectrum exhibits excess power near pump-referenced modes numbers  $\mu_{x,1} = 5 \times 24 = 120$  (1,547 nm) and  $\mu_{x,2} = 7 \times 24 = 168$  (1,541 nm). Also visible is suppressed comb generation where

the comb-resonator detuning has been increased. Here 24 FSR is the spacing of the prominent primary-comb lines.

### 2.1.1 Simulation of soliton crystals

To incorporate the stabilization mechanism described above into numerical simulations, we incorporate into the LLE a reduced comb-resonator detuning on a single mode  $\mu_x$ . The mode-dependent comb-resonator detuning can be calculated as:

$$\alpha_\mu = -2(\Omega_0 - D_1 + \omega_\mu)/\Delta\omega, \quad (2.1)$$

$$= \alpha - \beta\mu^2/2. \quad (2.2)$$

Here  $\Omega_0$  is the frequency of the pump laser,  $\omega_\mu$  is the set of cavity resonance frequencies referenced to the pumped mode, and  $D_1 = \partial\omega_\mu/\partial\mu|_{\mu=0}$  is the resonator's FSR at the pumped mode and is also assumed to be the Kerr-comb's repetition rate. The dispersion operator is applied in the frequency domain in numerical simulations of the LLE (see ??), which facilitates inclusion of  $\delta$ -function perturbations to the comb-resonator detuning as:

$$\alpha_\mu = \alpha - \beta\mu^2/2 + \Delta\alpha_\mu, \quad (2.3)$$

where

$$\Delta\alpha_\mu = 2(\omega_\mu - \omega_{\mu,0})/\Delta\omega \quad (2.4)$$

is the normalized change in the frequency of mode  $\mu$  from the expected frequency  $\omega_{\mu,0}$ .

We demonstrate the stabilization mechanism and the simulation method by presenting a simulation of the crystal in Fig. 2.1c. The simulation is shown in Fig. ???. This figure illustrates that, without the stabilization mechanism, the crystal will collapse. We note that a phenomenological application of coupled-mode theory[**Haus1991**] could be used to calculate the full perturbation to the soliton spectrum by the mode crossing, but we find that to explain the existence of this 23-soliton crystal and the apparently exact circumferential spacing of the pulses by  $2\pi/24$  radians, it is sufficient to incorporate into the LLE a reduced combresonator detuning on only mode 120 or

on mode 168, where the excess power is largest. The crystal is then a steady-state solution of the resulting perturbed LLE.

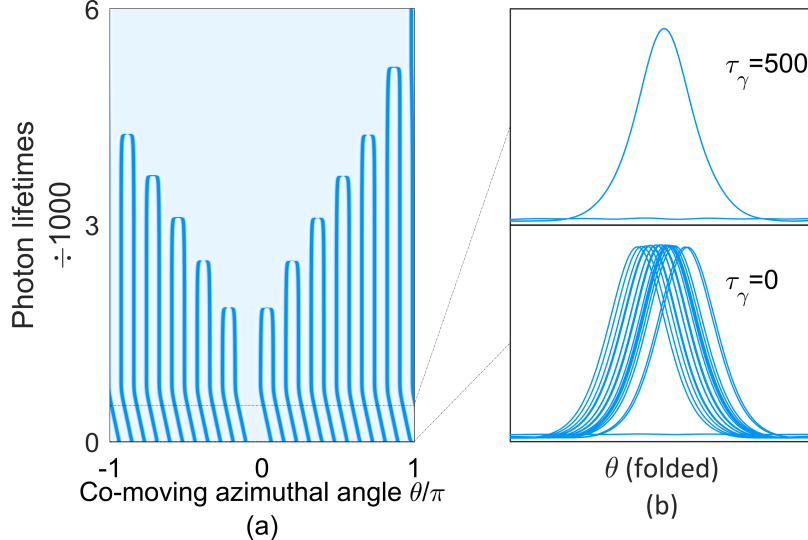


**Figure 2.2: Stabilization and collapse of a soliton crystal.** (a) Simulated evolution of the pulse train corresponding to the experimental crystal spectrum shown in Fig. 2.1c, starting from irregular pulse positions. For the first 500 photon lifetimes of the simulation, the propagation is governed by a perturbed LLE including reduced comb-resonator detuning on modes  $\mu_{x,1} = 120$  and  $\mu_{x,2} = 168$ . The soliton ensemble crystallizes within 10 seconds of initialization of the simulation, and then drifts within the co-rotating frame because the additional CW light on modes  $\mu_{x,1}$  and  $\mu_{times,2}$  correspond to traveling waves. The reduced comb-resonator detuning is removed smoothly from 500 to 1000 photon lifetimes, resulting in the destabilization of the crystal and pair-wise annihilation of the solitons. (b) Intracavity power with the azimuthal coordinate folded modulo  $2\pi/24$ , demonstrating the initial irregularity of the pulse positions and the crystallized pulse train after 500 photon lifetimes.

## 2.2 Case study: pair distribution function for a superstructured crystal

We consider a second specific example of a soliton crystal. The measured optical spectrum for this crystal is shown in Fig. 2.3a. This crystal exhibits superstructure—the soliton pulse train is nearly periodic in a small unit cell but is modulated with a larger periodicity. This results from the frustrated uniform distribution of 16 solitons with allowed inter-soliton separations of  $2\pi n/49$  radians; one pair is spaced by  $4 \times 2\pi/49$  instead of  $3 \times 2\pi/49$  radians. Excess power is apparent in the spectrum at mode  $\mu_x = 49$  (highlighted by the red circle in the plot), and we simulate this crystal by phenomenologically reducing the comb-resonator detuning on mode 49 so that the experimental

and simulated spectra agree. The background wave resulting from the constructive interference of the extended waves of the solitons, each having an angular period of  $2\pi/49$ , is visible in the plots of the simulated intensity in Fig. 2.3b and c.

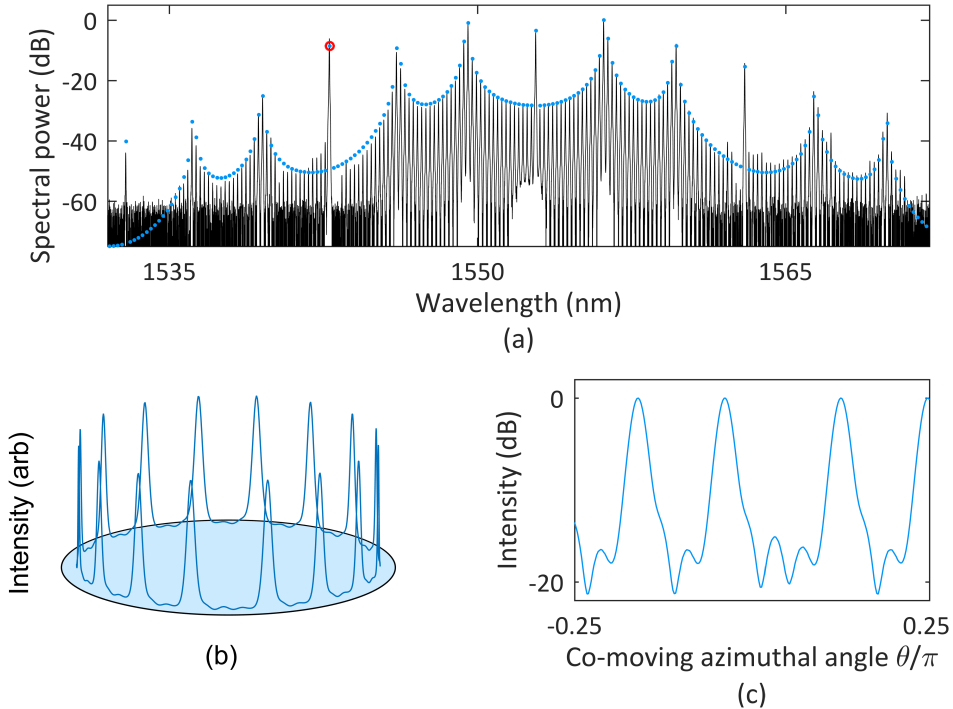


**Figure 2.3: Spectrum and waveform of a superstructured soliton crystal.** (a) Experimental (black) and simulated (blue) optical spectra of a superstructured crystal, with the red dot indicating the location of the mode crossing as described in the text. (b) Simulated time-domain intensity of frustrated-uniform distribution of 16 solitons over 49 lattice points. (c) Zoomed-in logarithm-scale plot of the same that clearly shows unoccupied lattice sites and the anomalous  $4 \times 2\pi/49$  spacing between a pair of pulses.

To gain insight into crystal generation, we simulate laser frequency scans across the resonance that generate this crystal in the presence of the mode crossing on mode 49. Example scans are shown for the case without the mode crossing (green) and with it (blue) in Fig. 2d. In both scans, solitons emerge from chaos as the frequency of the laser is decreased. In the presence of the mode crossing, they are generated with inter-soliton separations of  $2\pi n/49$  radians. A greater number of solitons emerge from chaos in the presence of the mode crossing, and this higher number helps to stabilize the crystal against thermal changes in the experiment. Further, upon continuation of

the simulation, some of the solitons in the scan without the mode crossing interact attractively and pair-annihilate, while the crystallized ensemble resulting from the scan with the mode crossing remains stable indefinitely.

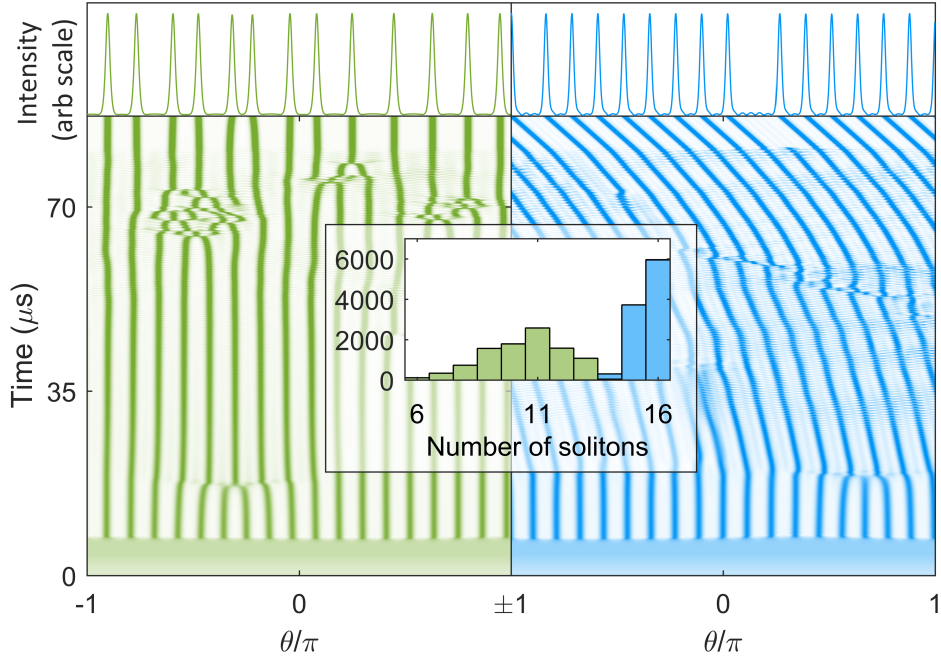


**Figure 2.4: Simulated generation of a superstructured soliton crystal.** Bottom: plots of the intracavity power during a simulated scan across the resonance, without (green) and with (blue) a mode crossing on mode 49 that reduces the comb-resonator detuning and increases the efficiency of frequency conversion on that mode. Top: final waveforms. Inset: histogram of the number of solitons generated in 10,000 simulated scans.

We investigate the pair-distribution function (PDF) for the soliton ensembles generated by these scans. The PDF is the probability that a soliton exists at position  $\theta_0 + \Delta\theta$  given that a different soliton exists at position  $\theta_0$ , normalized to the density. This is a useful metric to classify particle interactions which we borrow from condensed matter physics (see e.g. Ref. [42], especially Fig. 2, and Ref. 43, especially Fig. 1.1 and Chapter 3). We note that for numerically calculated discrete PDFs the absolute scaling of the PDF is not important, as it depends on the density of numerical sampling. In Fig. 2e, we plot the average PDFs for 10000 simulated scans with and without the mode crossing. The result for the case with a mode crossing is sharply peaked, indicating that

the allowed inter-soliton separations take on discrete values. The result for the case without the mode crossing is continuous, with a peak near the most likely nearest-neighbour separation and periodic revivals at its multiples, falling to the value of the PDF for uncorrelated soliton positions (the density) at large separations. This is exactly the expected form of the PDF for a liquid [42, 43]. For comparison, we plot a PDF (black, Fig. 2e) generated by simulation of a simple particle ensemble with mean inter-particle separation of  $\Delta\theta = 0.155\pi$  and normally distributed noise on this value with standard deviation of  $\sigma_{\delta\theta} = 0.18\Delta\theta$ . Thus, with a particle labelled by  $n = 0$  fixed at  $\theta = 0$ , the position of particle  $n$  is  $\theta_0 = n\Delta\theta + \Sigma_n \delta\theta_i$ , with  $\delta\theta_i$  the instantiations of the random variable representing the noise on the pulse spacings.

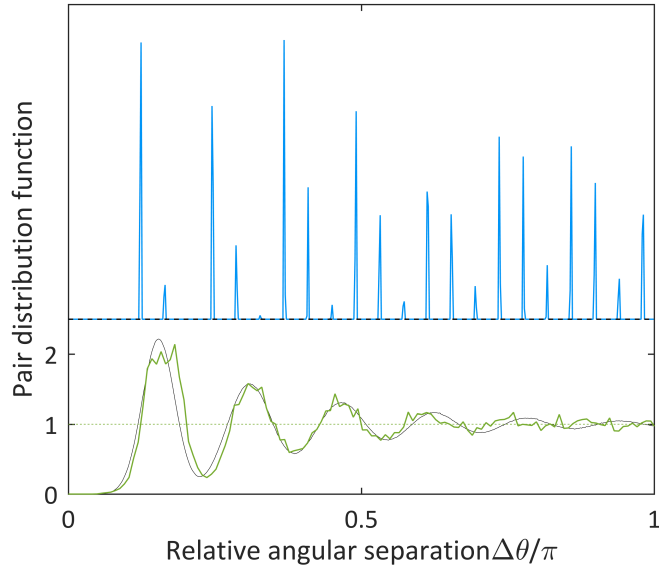


**Figure 2.5: Pair distribution function for soliton crystal generation.** Average pair-distribution functions calculated over 10,000 simulated scans across the resonance with (blue) and without (green) a mode crossing on mode 49. The width of the peaks in the discrete PDF is a single  $\Delta\theta$  bin. The expected PDF of a simple one-dimensional liquid (see main text) is plotted for comparison in black.

## 2.3 Soliton crystal configuration space

We observe a rich variety of soliton crystals explained by ordering in accordance with an extended background wave as described above; many of the optical spectra are plotted in Fig. 3. Op-

erationally, we adjust the pump laser power to provide repeatable conditions for creating particular crystals; more complex crystals occur with increased laser power, which intensifies the fluctuations in the chaos that precedes crystal generation and provides less well-ordered initial conditions. Once a crystal is generated, it is stable to small adjustments in the pump power and detuning, as the crystal structure is determined by the initial conditions for soliton formation rather than by an explicit dependence on pump power or detuning. The crystals we observe exhibit vacancies (Schottky defects)[27], Frenkel defects[27], disorder, or superstructure, or some combination thereof. A Frenkel defect consists of the shifting of a soliton in an otherwise uniform crystal. Disordered crystals are crystals in which the solitons fall on the peaks of the extended background wave, but their distribution across these peaks varies without any apparent regular order or favoured period.

We highlight the crystal plotted in Fig. 3n. This crystal exhibits both superstructure, with a superlattice period of  $2\pi/3$  radians, and a Frenkel defect. Three identical supercells per resonator round-trip yield a spectrum which has light in optical modes spaced by three resonator FSR, because the waveforms period has been reduced threefold. The Frenkel defect, occurring once per round-trip, contributes the single-FSR lobes to the spectrum. The result is three bursts of 8, 9, and 10 solitons respectively.

Fig. 3o shows a soliton crystal with inter-soliton separations that are slightly irregular and which we have not simulated as a steady-state solution of any perturbed LLE. We expect that the formation of the crystal and the distribution of solitons are dictated by mode interactions, but that in this case our simple approximation of a perturbation to the LLE by a reduced comb-resonator detuning on a single comb mode is not appropriate. Finally, we highlight the series of crystals plotted in Figs. 3p-3t. This series of crystals was generated by moving the pump laser closer to a mode-crossing in steps of integer multiples of the resonator FSR. This data demonstrates the influence of the background beating between the pump laser and the mode-crossing in determining the configuration of solitons in the resonator.

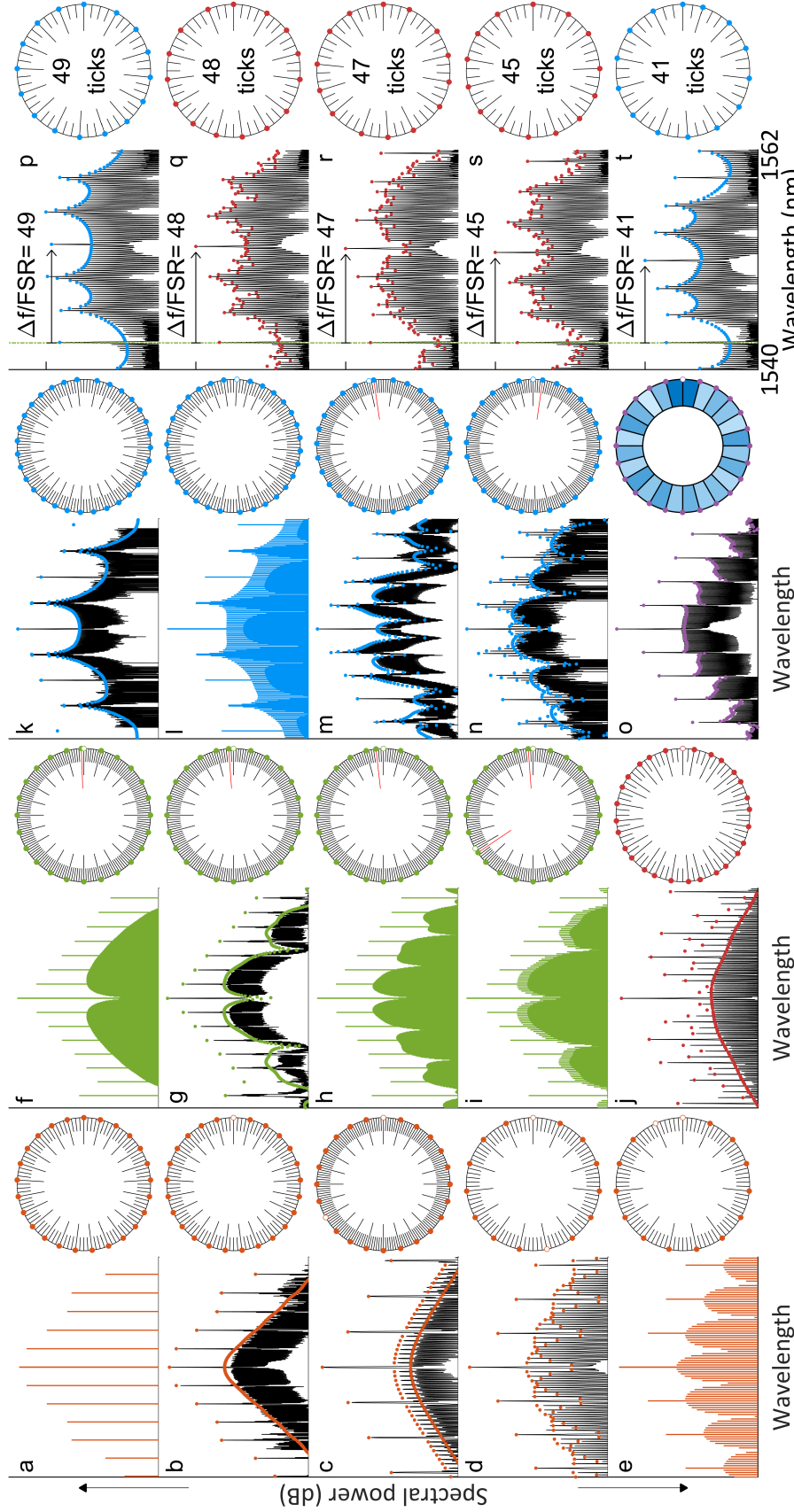


**Figure 2.6: Taxonomy of soliton crystals.** Measured optical spectra are shown in black, with simulations in color. Schematic depictions of the soliton distribution in the resonator co-moving frame are shown to the right of each spectrum. Major ticks in the schematic diagrams indicate the location or expected location of a soliton. Minor ticks indicate lattice sites, corresponding to peaks of the extended background wave due to a mode crossing. (a) A perfect soliton crystal, consisting of 25 uniformly-distributed solitons. (b-e) Soliton crystals exhibiting vacancies. (f-i) Soliton crystals exhibiting Frenkel defects. Shifted solitons still occupy a lattice site. (j) A disordered crystal. (k-n) Crystals exhibiting superstructure. (o) A crystal with irregular inter-soliton spacings. Darker shading indicates a smaller inter-soliton spacing. The range is inter-soliton spacings in 3 % of the mean. (p-t) A series of crystals generated as the pump laser is moved progressively closer to the stabilizing mode crossing.

## References

- [1] H. Taheri, A. A. Eftekhar, K. Wiesenfeld, and A. Adibi. Soliton formation in whispering-gallery-mode resonators via input phase modulation. *IEEE Photonics Journal*, 7 (2), **2015**, 2200309. DOI: [10.1109/JPHOT.2015.2416121](https://doi.org/10.1109/JPHOT.2015.2416121) (cited on pages 1, 5).
- [2] J. K. Jang, M. Erkintalo, S. Coen, and S. G. Murdoch. Temporal tweezing of light through the trapping and manipulation of temporal cavity solitons. *Nature Communications*, 6, **2015**, 7370. DOI: [10.1038/ncomms8370](https://doi.org/10.1038/ncomms8370). arXiv: [1410.4836](https://arxiv.org/abs/1410.4836) (cited on pages 2, 4, 6).
- [3] D Ceolto, A Bendahmane, J Fatome, G Millot, T Hansson, D Modotto, S Wabnitz, and B Kilber. Multiple four-wave mixing and Kerr combs in a bichromatically pumped nonlinear fiber ring cavity. *Optics Letters*, 41 (23), **2016**, 5462–5465 (cited on page 4).
- [4] Y. Wang, B. Garbin, F. Leo, S. Coen, M. Erkintalo, and S. G. Murdoch. Writing and Erasure of Temporal Cavity Solitons via Intensity Modulation of the Cavity Driving Field. *arXiv*, **2018**, 1802.07428. arXiv: [1802.07428](https://arxiv.org/abs/1802.07428) (cited on page 4).
- [5] H. Lee, T. Chen, J. Li, K. Y. Yang, S. Jeon, O. Painter, and K. J. Vahala. Chemically etched ultrahigh-Q wedge-resonator on a silicon chip. *Nature Photonics*, 6 (6), **2012**, 369–373. DOI: [10.1038/nphoton.2012.109](https://doi.org/10.1038/nphoton.2012.109). arXiv: [1112.2196](https://arxiv.org/abs/1112.2196) (cited on page 4).
- [6] J. R. Stone, T. C. Briles, T. E. Drake, D. T. Spencer, D. R. Carlson, S. A. Diddams, and S. B. Papp. Thermal and Nonlinear Dissipative-Soliton Dynamics in Kerr Microresonator Frequency Combs. *arXiv*, **2017**, 1708.08405. URL: <http://arxiv.org/abs/1708.08405>. arXiv: [1708.08405](https://arxiv.org/abs/1708.08405) (cited on page 4).
- [7] M. Zajnulina, M. Böhm, D. Bodenmüller, K. Blow, J. C. Boggio, A. Rieznik, and M. Roth. Characteristics and stability of soliton crystals in optical fibres for the purpose of optical frequency comb generation. *Optics Communications*, 393 (November 2016), **2017**, 95–102. DOI: [10.1016/j.optcom.2017.02.035](https://doi.org/10.1016/j.optcom.2017.02.035) (cited on page 11).
- [8] A. Haboucha, H. Leblond, M. Salhi, A. Komarov, and F. Sanchez. Coherent soliton pattern formation in a fiber laser. *Optics Letters*, 33 (5), **2008**, 524–526. DOI: [10.1364/OL.33.000524](https://doi.org/10.1364/OL.33.000524) (cited on page 11).
- [9] F. Amrani, M. Salhi, P. Grelu, H. Leblond, and F. Sanchez. Universal soliton pattern formations in passively mode-locked fiber lasers. *Optics letters*, 36 (9), **2011**, 1545–1547. DOI: [10.1364/OL.36.001545](https://doi.org/10.1364/OL.36.001545) (cited on page 11).

- [10] A. Haboucha, H. Leblond, M. Salhi, A. Komarov, and F. Sanchez. Analysis of soliton pattern formation in passively mode-locked fiber lasers. *Physical Review A*, 78, **2008**, 043806. DOI: [10.1103/PhysRevA.78.043806](https://doi.org/10.1103/PhysRevA.78.043806) (cited on page 11).
- [11] B. A. Malomed, A Schwache, and F Mitschke. Soliton lattice and gas in passive fiber-ring resonators. *Fiber and Integrated Optics*, 17 (4), **1998**, 267–277. DOI: [10.1080/014680398244867](https://doi.org/10.1080/014680398244867) (cited on page 11).
- [12] F. Mitschke and A. Schwache. Soliton ensembles in a nonlinear resonator. *Journal of Optics B: Quantum and Semiclassical Optics*, 10 (6), **1998**, 779–788 (cited on page 11).
- [13] A. Schwache and F. Mitschke. Properties of an optical soliton gas. *Physical Review E*, 55 (6), **1997**, 7720–7725. DOI: [10.1103/PhysRevE.55.7720](https://doi.org/10.1103/PhysRevE.55.7720) (cited on page 11).